



Impacts of drought and heatwave on the terrestrial ecosystem in China as revealed by satellite solar-induced chlorophyll fluorescence

Xiaorong Wang ^{a,b}, Bo Qiu ^{a,b,*}, Wenkai Li ^c, Qian Zhang ^{a,b}

^a Jiangsu Provincial Key Laboratory of Geographic Information Science and Technology, International Institute for Earth System Sciences, Nanjing University, Nanjing, China

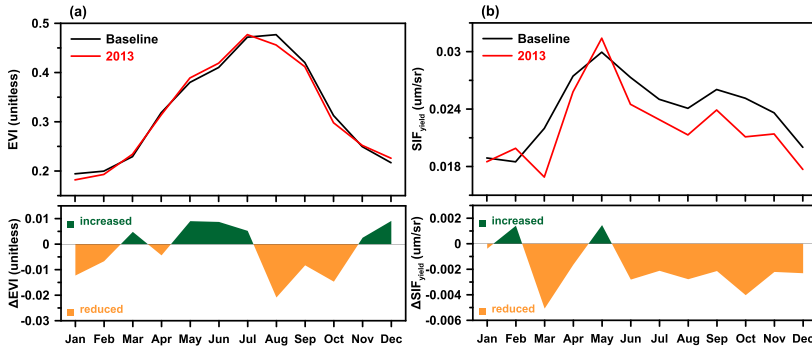
^b Jiangsu Center for Collaborative Innovation in Geographical Information Resource Development and Application, Nanjing, China

^c Key Laboratory of Meteorological Disaster, Ministry of Education (KLME)/Joint International Research Laboratory of Climate and Environment Change (ILCEC)/Collaborative Innovation Center on Forecast and Evaluation of Meteorological Disasters (CIC-FEMD), Nanjing University of Information Science & Technology, Nanjing, China

HIGHLIGHTS

- Dynamics of 2009/2010 drought and the 2013 heatwave in China are investigated.
- SIF_{yield} shows earlier responses to drought and heatwave than traditional VIs.
- SIF_{yield} is more sensitive to high VPD than low soil moisture.

GRAPHICAL ABSTRACT



ARTICLE INFO

Article history:

Received 9 May 2019

Received in revised form 23 July 2019

Accepted 26 July 2019

Available online 27 July 2019

Editor: Jay Gan

Keywords:

Solar-induced chlorophyll fluorescence

Drought

Heatwave

Vapor pressure deficit

Soil moisture

ABSTRACT

Droughts and heatwaves have been and will continue to bring large risks to terrestrial ecosystems. However, the understanding of how plants respond to drought and heatwave over broad spatial scales is still limited. In this paper, we use the 2009/2010 drought in Yunnan and the 2013 heatwave over southern China as case studies to investigate the potential of using satellite-observed solar-induced chlorophyll fluorescence (SIF) to monitor vegetation responses to drought and heatwave over broad spatial scales. The 2009/2010 drought onset follows a strong soil moisture deficit due to the yearlong below-normal precipitation in Yunnan from the autumn of 2009 to the spring of 2010. In the summer of 2013, southern China experienced the strongest heatwave due to the sudden temperature increase and rainfall deficit. The results show that SIF can reasonably capture the spatial and temporal dynamics of drought and heatwave development, as indicated by the large reduction in fluorescence yield (SIF_{yield}). Moreover, SIF_{yield} demonstrates a significant reduction and earlier response than traditional vegetation indices (enhanced vegetation index, EVI) during the early stages of drought and heatwave events. For both study areas, the spatial and temporal correlation analysis demonstrates that the SIF_{yield} anomalies are more sensitive to a high vapor pressure deficit (VPD) than low soil moisture. This study implies that satellite observations of SIF have great potential for accurate and timely monitoring of drought and heatwave developments.

© 2019 Elsevier B.V. All rights reserved.

* Corresponding author at: Jiangsu Provincial Key Laboratory of Geographic Information Science and Technology, International Institute for Earth System Sciences, Nanjing University, Nanjing, China.

E-mail address: qubo@nju.edu.cn (B. Qiu).

1. Introduction

Drought and heatwave, which are associated with below-normal precipitation or above-normal air temperatures sustained for months to years, have substantial impacts on agriculture, water resources, and human society. The occurrence and duration of droughts and heatwaves have substantially increased as a consequence of climate change (Dai, 2013; Trenberth et al., 2014; Wang et al., 2017a, 2017b). During the last two decades, many droughts and heatwaves with longevity and widespread spatial extent have occurred over different regions across the globe, such as North China from 1999 to 2001 (Zhang and Zhou, 2015), Europe in 2003 (Ciais et al., 2005), North America from 2011 to 2012 (Sun et al., 2015), and tropical regions from 2015 to 2016 (Qian et al., 2019; Yang et al., 2018; Zhang et al., 2018). Therefore, droughts and heatwaves are among the most damaging extreme climate events at both the regional and global scales.

Water and carbon cycles are strongly coupled in terrestrial ecosystems through vegetation photosynthesis (Lee et al., 2013; Qiu et al., 2018; Yoshida et al., 2015). Higher air temperature and below-normal precipitation usually occur during drought and heatwave periods. The cellular injury of plants occurs in response to extremely high temperatures over a short time, especially during the growing season (Song et al., 2018). The exposure of plants to high temperatures will lead to a decline in vegetation productivity (Al-Khatib and Paulsen, 1990). In addition, reduced precipitation is associated with a large decrease in soil moisture and results in a water deficit for vegetation growth. Plant photosynthesis responds to water deficits through reductions in stomatal conductance, which could prevent water loss (Katul et al., 2009). At the global scale, extreme droughts have reduced the net primary productivity (NPP) and have weakened the terrestrial carbon sink (Zhao and Running, 2010). The impacts of droughts and heatwaves on terrestrial carbon budgets have also been reported in different regions. In North America, the extreme drought in the central Great Plains in 2012 substantially reduced the vegetation production and led to a significant decrease in crop yield (Sun et al., 2015; Wolf et al., 2016). In Amazon, the drought induced by a strong El Niño event during 2015 and 2016 strongly decreased the gross primary production (GPP) and resulted in reductions in the net carbon uptake of terrestrial ecosystems (Qian et al., 2019; Yang et al., 2018). Alterations to the regional carbon cycle due to droughts and heatwaves can also be found in some other regions across the globe (Reichstein et al., 2007; Yoshida et al., 2015; Yuan et al., 2016).

Traditional greenness-based vegetation indices (VIs), such as the normalized difference vegetation index (NDVI) and enhanced vegetation index (EVI), have been widely used to evaluate the impacts of water and heat stress on vegetation productivity during large-scale droughts and heatwaves (Xu et al., 2011; Zhou et al., 2014). The estimations of potential photosynthesis from VIs are used to effectively understand the response of vegetation growth to droughts. However, these traditional greenness-based VIs only relate to the potential photosynthesis, not the actual processes. In addition, VIs have difficulty showing the accurate response of plants to environmental stresses (Meroni et al., 2008). Therefore, a new way of estimating photosynthetic activity is needed for monitoring the vegetation response to droughts and heatwaves at the regional and global scales.

Recent developments in solar-induced chlorophyll fluorescence (SIF) have provided a novel approach to estimate terrestrial photosynthesis. The solar radiation absorbed by chlorophyll molecules is transferred to the provide energy for photosynthesis, dissipated as heat or re-emitted as SIF (Porcar-Castell et al., 2014). Therefore, SIF can be used as a direct link to the actual photosynthetic processes. SIF is closely related to GPP among various vegetation types and can respond rapidly to the environmental stress (Guan et al., 2016; Lee et al., 2013; Song et al., 2018). However, greenness-based VIs are not so sensitive to changes in water or temperature conditions because of the indirect link to actual photosynthesis in plants. Lee et al. (2013) demonstrated

that satellite SIF data exhibit a clear response to water deficits over tropical rainforests; however, NDVI does not capture the water stress signals well. In croplands, Song et al. (2018) found that SIF products showed a substantial decrease and earlier response to heat stress, while NDVI and EVI captured these signals one month later. Satellite-based SIF data have also been shown to be more sensitive to environmental stress than greenness-based VIs (Guan et al., 2016; Lee et al., 2013; Sun et al., 2015; Yoshida et al., 2015).

The frequency of extreme drought and heatwave events has increased significantly during recent decades and has had substantial impacts on the ecosystems in southern China (Yuan et al., 2016; Zhang et al., 2012). The severe drought from the autumn of 2009 to the spring of 2010 led to economic losses of about USD 30 billion in southwestern China (Zhang et al., 2012; Zhang and Zhou, 2015). In addition, the 2013 summer heatwave in southern China induced much higher air temperature than the long-term mean, breaking the historical record (Yuan et al., 2016). Therefore, the 2009/2010 drought in Yunnan and the 2013 heatwave over the southern China are selected as case studies to investigate the potential of using satellite-observed SIF to monitor vegetation responses to drought and heatwave in China. The goals of this study are to advance the understanding of how the spatial and temporal dynamics of SIF are related to those of various climatic variables and the differences in the responses of SIF and traditional VIs to drought and heatwave under these two regimes.

2. Materials and methods

2.1. Study area

In this paper, the drought and the heatwave are investigated in Yunnan and southern China, respectively. These two study areas are located in southwest and southern China (Fig. S1). For the drought region, approximately 70% of the area is covered by forests according to the MODIS land cover product (MCD12Q1). The heatwave region includes 9 provinces and 2 provincial municipalities in southern China. According to the MODIS land cover product, forests (43%) and croplands (40%) are the dominant vegetation types in the study area. These two study areas are dominated by forests and croplands, therefore, both play important roles in food supply and carbon uptake in China.

2.2. Meteorological data

The daily mean temperature (°C), precipitation (mm) and relative humidity (%) at 839 national meteorological stations across China from 2007 to 2016 are collected from the National Meteorological Information Center of China Meteorological Administration (<http://data.cma.cn/>). These meteorological station data are quality controlled (Li et al., 2004) and have been widely used in previous studies on extreme climatic events in China (Wang et al., 2017a, 2017b). We use the temperature and relative humidity station data to calculate the vapor pressure deficit (VPD).

2.3. Satellite SIF and vegetation indices

In this study, we use SIF data products from the GOME-2 datasets, which provide SIF observations with the longest duration and highest fidelity at the global scale (Joiner et al., 2013). The monthly mean SIF data retrieved from the red band at 0.5° spatial resolution were collected from 2007 to 2016. The red SIF data were prescreened for clouds by filtering out pixels with effective cloud fractions of >30%. In addition, the GOME-2 SIF products were partially filtered by eliminating pixels with solar zenith angles >70° to minimize the data uncertainties. More detailed descriptions of the retrieval method can be found in (Joiner et al., 2013, 2016). A decreasing trend is exhibited in the GOME-2 SIF measurements, which is caused by sensor degradation (Zhang et al.,

2018). Therefore, the detrending method is used to minimize the uncertainty in satellite SIF data (Qiu et al., 2019).

Monthly photosynthetic active radiation (PAR) datasets at 1° spatial resolution are collected from the NASA Langley Research Center, Cloud and Earth's Radiant Energy System (CERES). CERES datasets provide global radiative fluxes with long-term durations to examine the radiation budget at Earth's surface (Dong et al., 2008). In this study, the total PAR is calculated by the sum of surface direct and diffusive PAR in all sky conditions (Yang et al., 2018).

The MODIS EVI datasets are collected from the Land Processes Distributed Active Archive Center. We use the monthly mean 0.05° spatial resolution EVI data from 2007 to 2016. The EVI datasets are quality filtered for clouds by excluding pixels contaminated by clouds and aerosols based on the quality flags. Due to the key influences of solar radiation on SIF, the MODIS fraction of PAR (fPAR), which represents the proportion of available radiation absorbed by vegetation canopies, is used to reveal the effects of solar radiation variations on SIF dynamics. The MOD15A2 fPAR products used in this study are available at 1-km spatial resolution and 8-day temporal resolution (Myndeni et al., 2002).

The Global Inventory Modeling and Mapping Studies (GIMMS) NDVI datasets from the Advanced Very High Resolution Radiometer observation (AVHRR) instruments are collected from 2007 to 2015 (Pinzon and Tucker, 2014). The GIMMS NDVI datasets have a spatial resolution of 1/12° and a 15-day interval temporal resolution.

2.4. Soil moisture and terrestrial water storage

The soil moisture datasets are collected from the Climate Change Initiative (CCI) of the European Space Agency (ESA) to reveal the water conditions during droughts and heatwaves. The ESA CCI soil moisture products are merged from the retrievals of thirteen active and passive sensors (Liu et al., 2012). The daily mean soil moisture datasets at a spatial resolution of 0.25° are available from 2007 to 2016. These datasets have been proven to be consistent with in situ soil moisture observations (Dorigo et al., 2015). The soil moisture data from Global Land Evaporation and Amsterdam Model (GLEAM) are also used in this paper. GLEAM is a well-established land surface model and the input of GLEAM comes from different independent satellites data to generate global products, such as soil moisture, evapotranspiration and potential evaporation (Miralles et al., 2011; Martens et al., 2017). The GLEAM surface soil moisture data have a spatial resolution of 0.25° and a monthly temporal resolution from 2007 to 2016.

In this paper, we also use the terrestrial water storage (TWS) from the joint US-German (NASA-GFZ) Gravity Recovery and Climate Experiment (GRACE) satellite mission (Chen et al., 2004; Wahr et al., 2004). The GRACE satellite measures the variations in Earth's gravity field to monitor the total vertically integrated TWS, including the soil moisture in surface and deep layers, surface water reservoir storage, and groundwater storage. We collect the latest release of TWS data from the Jet Propulsion Laboratory (JPL) release 05 (RL05) at a spatial resolution of 1° from 2007 to 2016. Due to a "battery management" issue, the GRACE TWS dataset has missing data in some months.

2.5. Ground-based measurements

In this paper, the ground-based measurements of Lishui site from 2012 to 2013 are used to investigate the impacts of heatwave on the vegetation growth in southern China. The Lishui site (31.72°N, 118.98°E) is in the southern Jiangsu Province, China. The dominant species of this site is grass, which has an average height of approximately 60 cm. The annual air temperature is 15 °C, and the annual mean precipitation is over 1000 mm, of which about 50% typically falls during the monsoon period from June to August. More details on the site have been found in the previous studies (Guo et al., 2016; Wang et al., 2017a, 2017b).

2.6. Analysis

In this paper, the datasets have different temporal and spatial resolutions. To match the temporal and spatial resolutions of GOME-2 SIF, all the variables are aggregated into monthly composites at a 0.5° spatial resolution. To examine the differences between SIF and greenness-based VIs, two important variables are calculated when fPAR and PAR data are available. These two variables are SIF normalized by PAR (referred to as SIF_{PAR} hereafter) and absorbed photosynthetically active radiation (APAR) (referred to as SIF_{yield} hereafter) and can be expressed as follows:

$$SIF_{PAR} = SIF/PAR \quad (1)$$

$$SIF_{yield} = SIF/APAR = SIF/(fPAR \times PAR) \quad (2)$$

SIF_{PAR} and SIF_{yield} eliminate the effects of PAR and APAR on SIF and can be used to indicate the effective fluorescence yield and photosynthetic efficiency of plants. Droughts and heatwaves are generally accompanied by substantially increased solar radiation, which leads to higher PAR and APAR. Therefore, SIF_{PAR} and SIF_{yield} can be used to improve our understanding of SIF dynamics.

To examine the changes in the variables during drought and heatwave, the spatial anomalies are calculated in this paper. The standardized anomalies of all the variables are computed on a pixel-by-pixel basis. The standardized anomaly (referred to as anomaly henceforth) for each pixel during the drought or heatwave period is calculated as a departure from the multiyear mean and normalized by the standard deviation (SD) from 2007 to 2016:

$$var'(i,j,t) = \frac{var(i,j,t) - \bar{var}(i,j)}{SD(var(i,j,t))} \quad (3)$$

where $var'(i,j,t)$ is the standardized anomaly of pixel (i,j) at time t , $var(i,j,t)$ is the original value of pixel (i,j) at time t , $\bar{var}(i,j)$ is the mean value of pixel (i,j) from 2007 to 2016, $SD(var(i,j,t))$ is the standard deviation of pixel (i,j) from 2007 to 2016. For GIMMS NDVI, the mean value and standard deviation are calculated from 2007 to 2015.

To further quantify the spatial similarity of two variables, the spatial correlation coefficient (SCC) is calculated, as described in Section 3.3. The equation is described as follows:

$$SCC = \frac{\sum(x_{i,j} - \bar{x}) \cdot \sum(y_{i,j} - \bar{y})}{\sqrt{\sum(x_{i,j} - \bar{x})^2 \cdot \sum(y_{i,j} - \bar{y})^2}} \quad (4)$$

where $x_{i,j}$ and $y_{i,j}$ are the original values of pixel (i,j) , \bar{x} and \bar{y} are the spatially averaged values of the two variables.

3. Results

3.1. Spatiotemporal dynamics of the 2009/2010 drought in Yunnan

During the dry months from September 2009 to May 2010, the air temperature is much higher than the multiyear mean, with the largest positive anomalies >1 SD (Fig. 1a). Meanwhile, meteorological data also demonstrate that 78% of Yunnan shows precipitation anomalies less than -1 SD (Fig. 1c). As the temperatures increase and precipitation decreases, the entire region shows positive VPD and negative TWS anomalies. In addition, the SWC has large reductions, 80% and 85% of the area has SWC anomalies less than -1 SD for GLEAM and ESA data, respectively. The negative anomalies of SWC and TWS indicate substantial depletion in the surface and root zone soil water. During the drought period, the large precipitation reductions lead to substantial depletion in water storage and the persistence of hydrological drought in Yunnan.

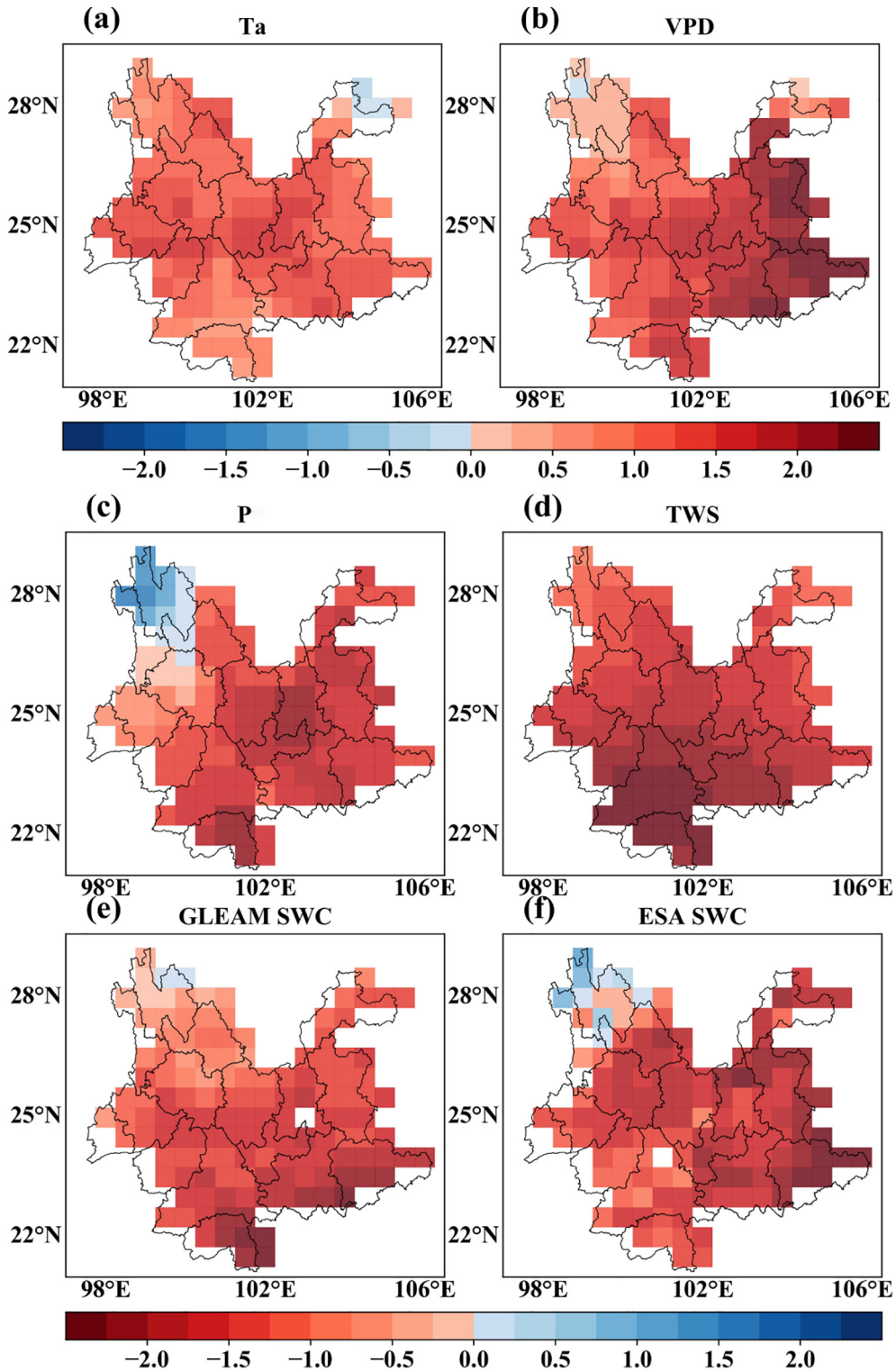


Fig. 1. The spatial distributions of the anomalies of (a) air temperature, (b) VPD, (c) precipitation, (d) TWS, (e) GLEAM SWC and (f) ESA SWC in Yunnan from September 2009 to May 2010.

The seasonal cycles of meteorological and hydrological variables during the dry months (August 2009 to July 2010) are shown in Fig. S2. The air temperature increases in most months from September 2009 to March 2010 (Fig. S2a). A negative precipitation anomaly lasts from autumn 2009 to spring 2010, with the largest precipitation reduction of 40% relative to the multiyear mean in September 2009 (Fig. S2c). The persistent precipitation reductions lead to increased atmospheric dryness and depletion in the soil moisture of the surface and deep layers. Much higher VPD (Fig. S2b) and lower TWS and SWC values

(Fig. S2d-f) are observed during the dry months in Yunnan. The largest VPD increase of 30% relative to the multiyear mean is found in September 2009. The spatial and temporal analysis showed that the precipitation deficit lasted for about 8 months in Yunnan and led to extreme drought persistence, which had large impacts on the vegetation growth in this region.

This 2009/2010 drought event in Yunnan is characterized by a persistent depletion of soil moisture induced by the yearlong below-normal precipitation from autumn 2009 to spring 2010. Compared to

the multiyear mean, the precipitation (temperature) is slightly lower (higher) in August and much lower (higher) in September and October, indicating that the drought starts in August and strengthens in the following two months. The regional anomalies of NDVI, EVI, SIF_{PAR} and SIF_{yield} in Yunnan from August to October are shown to investigate the dynamics of the vegetation responses during the drought (Fig. S3). In August 2009, most of Yunnan shows positive NDVI and EVI anomalies, while negative SIF_{PAR} and SIF_{yield} anomalies are found in approximately 48% of this area. With the development of water stress in Yunnan, over 40% of the vegetation in Yunnan suffers moderate (less than -0.5 SD) losses as indicated by SIF_{PAR} and SIF_{yield}, and over 20% of the vegetation suffers severe losses (less than -1 SD) in September. But most of Yunnan shows positive NDVI and EVI anomalies in September. As water stress expands and strengthens, approximately 80% of Yunnan suffers from water stress, as indicated by the SIF_{PAR} and SIF_{yield} values in October, while only 21% and 58% of the area suffers from NDVI and EVI losses. The spatial distributions of NDVI, EVI, SIF_{PAR} and SIF_{yield} anomalies indicate that the satellite observations of VIs are less sensitive to water stress than SIF_{PAR} and SIF_{yield}.

The seasonal cycles of NDVI, EVI, SIF_{PAR}, and SIF_{yield} during the drought period are shown in Fig. 2. The satellite observations of NDVI and EVI are higher than the multiyear mean in August of 2009 when the VPD and SWC start to respond to the precipitation deficit in Yunnan (Fig. 2). In September, the value of EVI is almost the same as the multiyear mean and the value of NDVI is still much higher than the multiyear

mean. As the drought evolves over the area, NDVI and EVI begin to exhibit a slightly negative response to drought in October (Fig. 2a–b). However, the SIF_{PAR} and SIF_{yield} show much larger reductions and more consistent declines with water stress than NDVI and EVI. The values of SIF_{PAR} and SIF_{yield} exhibit significant decreases in September relative to the multiyear mean, indicating the strong response of vegetation to water stress in Yunnan. Then the negative values of SIF_{PAR} and SIF_{yield} are observed throughout the following drought months. Overall, the analysis indicates that satellite SIF data can capture the water stress dynamics in Yunnan and are more sensitive to extreme drought conditions than traditional greenness-based VIs in terms of magnitude and temporal variations.

3.2. Spatiotemporal dynamics of the 2013 heatwave over southern China

The spatial distributions of air temperature, precipitation, VPD, TWS and SWC during the heatwave in southern China are shown in Fig. 3. Meteorological data show that 88% of southern China shows temperature anomalies >1 SD, and 32% of the area has anomalies >2 SD, indicating an extreme heatwave event from June to August in 2013 (Fig. 3a). Meanwhile, the precipitation is also less than the multiyear mean, with the largest negative anomalies less than -1 SD. The much higher air temperature will lead to a substantial increase in VPD and depletion in surface soil moisture. Therefore, the VPD shows that 89% of southern China has an anomaly of >1 SD, and 28% has an anomaly of >2 SD. In

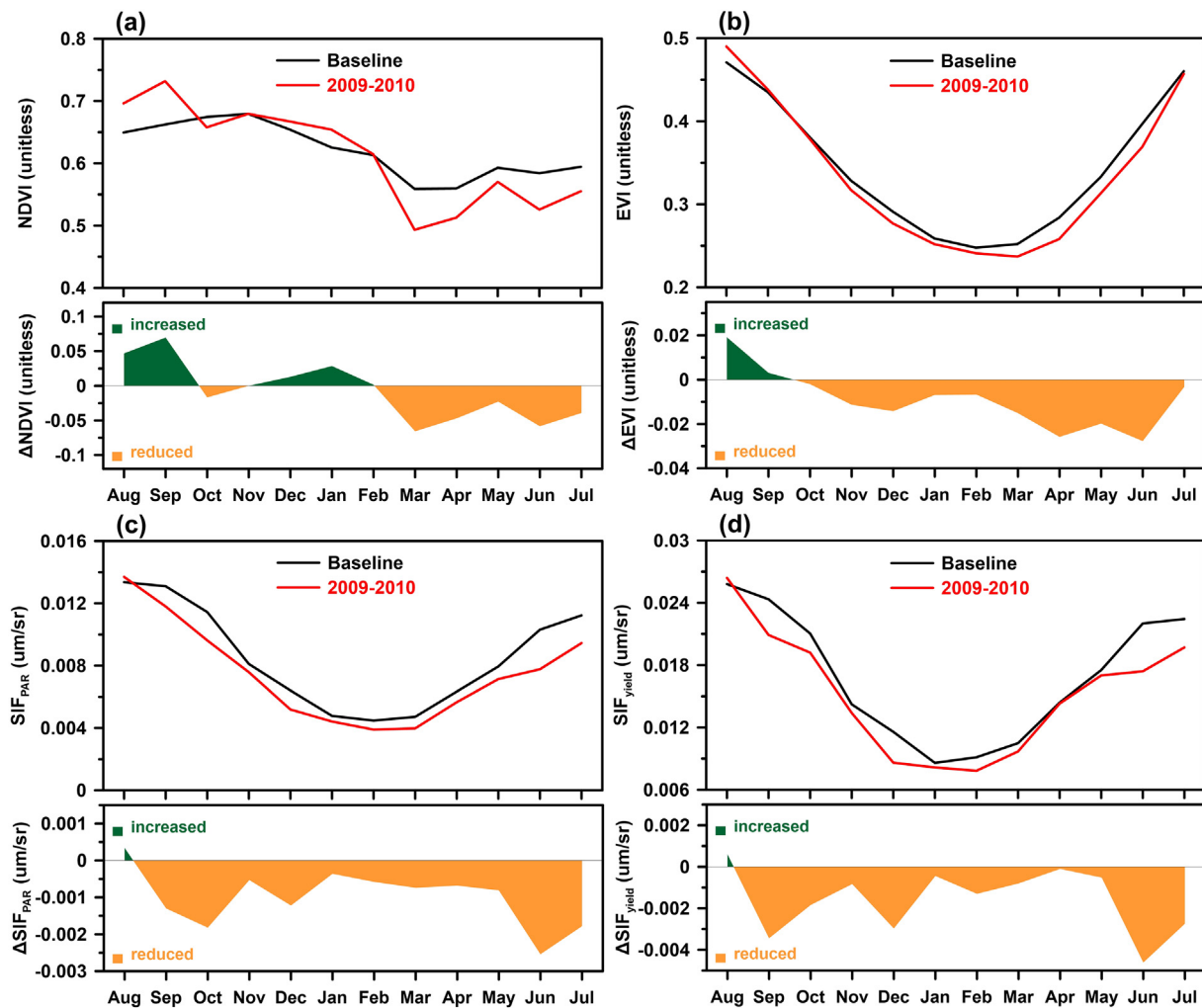


Fig. 2. The region-wide mean seasonal cycles and anomalies of (a) NDVI, (b) EVI, (c) SIF_{PAR} and (d) SIF_{yield} in Yunnan from August 2009 to July 2010. The black curves represent the monthly multiyear mean of each variable between 2007 and 2016; the red curves show the seasonal evolution during the drought period. (For interpretation of the references to colour in this figure legend, the reader is referred to the web version of this article.)

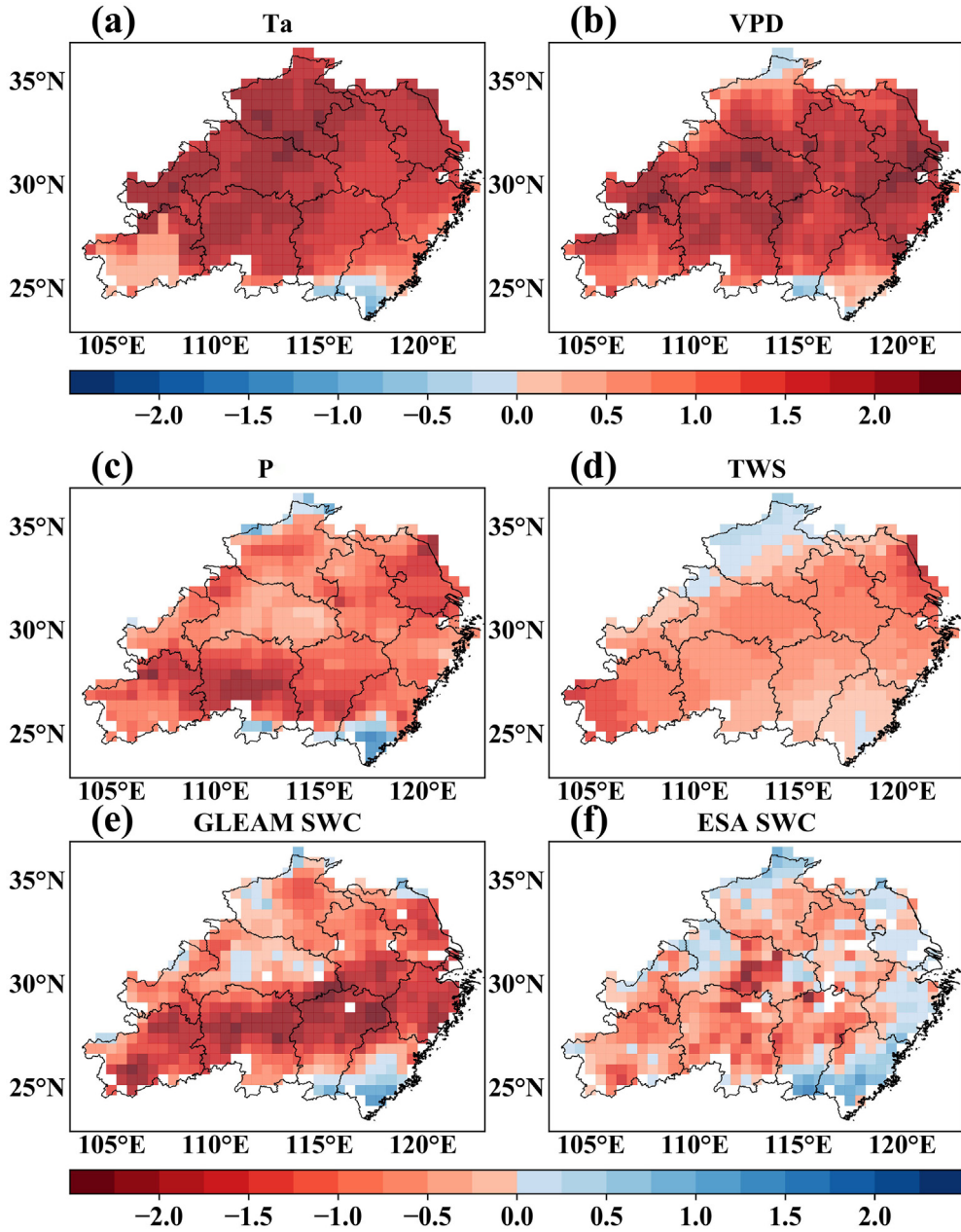


Fig. 3. The spatial distributions of the anomalies of (a) air temperature, (b) VPD, (c) precipitation, (d) TWS, (e) GLEAM SWC and (f) ESA SWC in southern China from June to August 2013.

addition, most of the area has negative TWS and SWC anomalies during the extreme heatwave. The heatwave, which is associated with much higher temperatures and reduced precipitation, leads to the persistence of heat stress and depletion of soil moisture in southern China.

The seasonal cycles of climatic variables relative to the multiyear means are shown in Fig. 4. Extremely high air temperatures are observed in most of southern China in 2013. The temperature is much higher than the multiyear mean in July and August (Fig. 4a). Meanwhile, the meteorological data also show that the precipitation reduction starts in June and the largest decrease in precipitation occurs in July, with a 40% reduction in precipitation compared to the multiyear mean (Fig. 4c). The extremely high temperatures and precipitation deficits lead to increases in the VPD and depletion of soil moisture in surface and root zone layers. Much higher VPD (Fig. 4b) and lower TWS and SWC values (Fig. 4d-f) are observed during the heatwave in southern China. The largest VPD exhibits an increase of 40% relative to the multiyear mean in August 2013. This heatwave event is characterized by sudden extremely high temperatures coupled with a precipitation deficit,

increased VPD and depleted soil moisture, leading to a rapid onset of heatwave in early summer over southern China.

Vegetation growth is strongly affected by heat stress in southern China. The spatial distributions of greenness-based VIs and SIF are shown to investigate the responses of vegetation to heat stress in southern China. During the extreme heatwave event, the precipitation exhibits a sudden decrease in June, and the high air temperature starts in June and peaks in July and August in 2013. The spatial distributions of NDVI, EVI, SIF_{PAR} and SIF_{yield} anomalies in southern China from June to August are shown in Fig. 5. Most of the study area shows positive anomalies of NDVI and EVI in June at the beginning of the heatwave. However, over 60% and 70% of this area appear to exhibit negative SIF_{PAR} and SIF_{yield} anomalies, respectively. As heat stress expands and strengthens in southern China, over 40% of the vegetation in southern China experience moderate (less than -0.5 SD) losses of SIF_{PAR} in July 2013 and over 18% of the vegetation experiences severe losses (less than -1 SD). And the percentages of moderate and severe SIF_{yield} losses are 47% and 21%, respectively. However, only 25% and 8% of the area

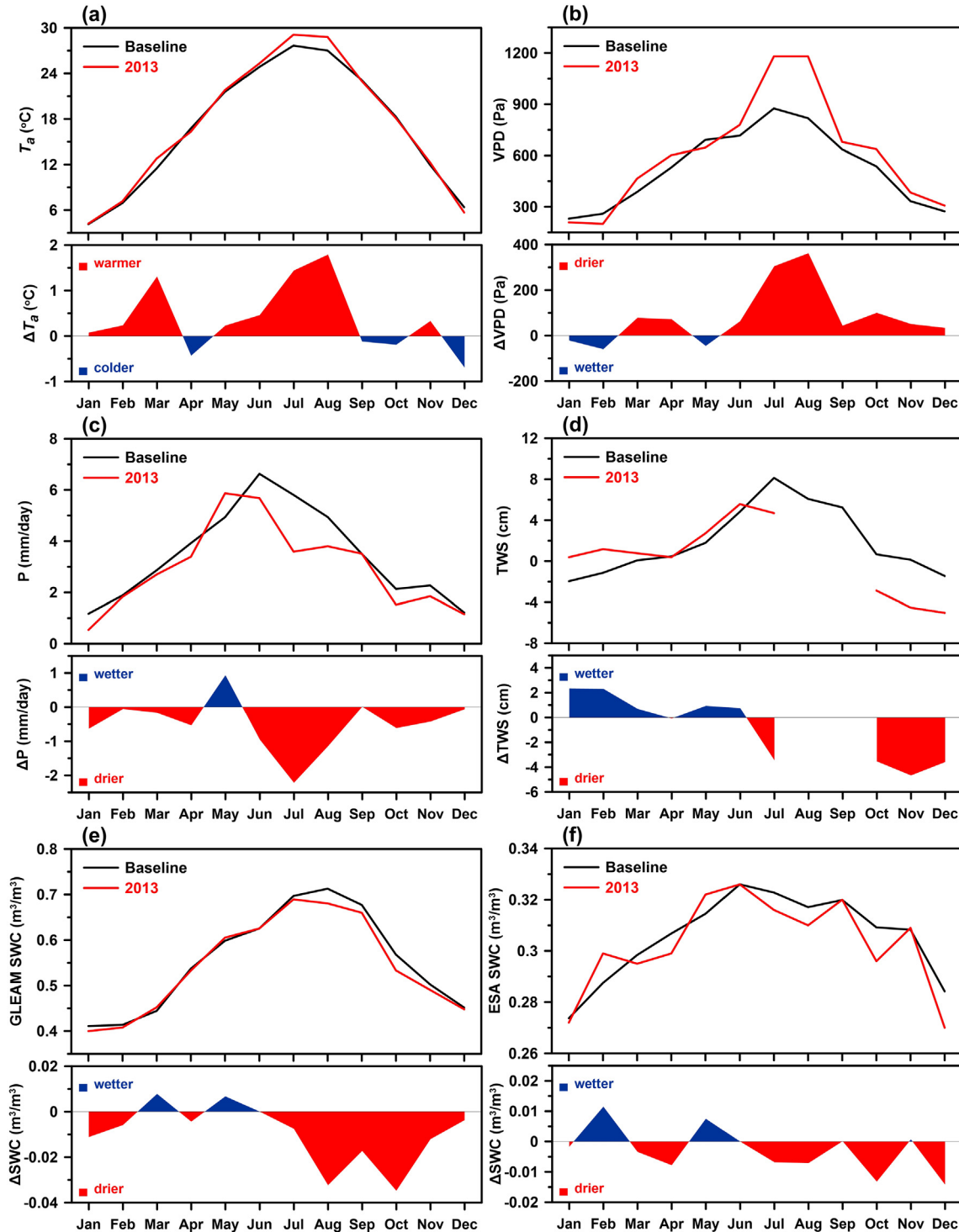


Fig. 4. The region-wide mean seasonal cycle and anomalies of (a) air temperature, (b) VPD, (c) precipitation, (d) TWS, (e) GLEAM SWC and (f) ESA SWC for southern China in 2013. The black curves represent the monthly multiyear mean of each variable between 2007 and 2016; the red curves show the seasonal evolution during the heatwave period. (For interpretation of the references to colour in this figure legend, the reader is referred to the web version of this article.)

experience moderate and severe EVI losses, which underestimate the losses by 50% relative to the SIF observations. At the end of this heatwave, most of southern China suffers from heat stress, as indicated by EVI, SIF_{PAR} and SIF_{yield} in August, whereas the negative anomalies are less widespread for EVI than the other two indicators. A positive NDVI anomaly appears in most of the southern China in July and August. The spatial distributions of NDVI, EVI, SIF_{PAR} and SIF_{yield} indicate that the satellite observations of SIF show higher sensitivity to heat stress than greenness-based VIs.

The seasonal cycles of NDVI, EVI, SIF_{PAR}, and SIF_{yield} during the extreme heatwave are shown in Fig. 6. The NDVI shows higher values than the multiyear mean during the extreme heatwave in southern China, indicating the weak response to the heat stress. The value of EVI is slightly higher than the multiyear mean in June when the air temperature starts to increase and the precipitation decreases in southern China (Fig. 6b). In addition, the value of EVI is close to the multiyear mean although the heat stress peaks in July. As the heat stress expands over the entire region, EVI begins to exhibit negative responses to the

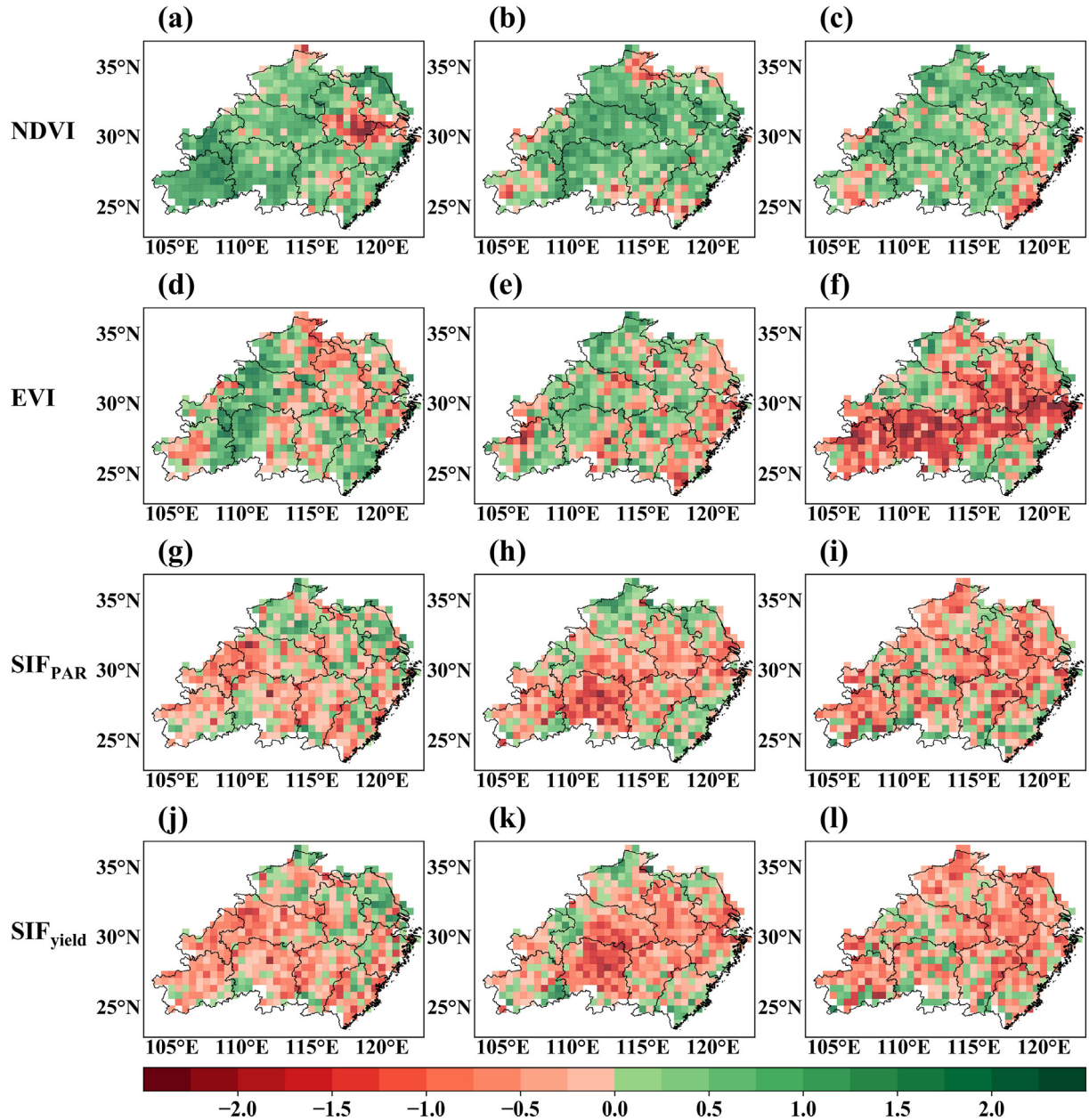


Fig. 5. The spatial distributions of the anomalies of (a–c) NDVI, (d–f) EVI, (g–i) SIF_{PAR} and (j–l) SIF_{yield} over southern China in June (left column), July (middle column) and August (right column) in 2013.

heatwave in August. However, the SIF_{PAR} and SIF_{yield} show much larger reductions and more consistent declines with heat stress relative to that of EVI (Fig. 6c–d). The values of SIF_{PAR} and SIF_{yield} are lower in June relative to the multiyear mean, indicating that the vegetation starts to respond to the heat stress in southern China. Then, the SIF_{PAR} and SIF_{yield} losses expand in July and peak in August 2013. Therefore, the spatial and temporal analyses show that SIF_{PAR} and SIF_{yield} are better indicators than NDVI and EVI for capturing the dynamic process of heat stress evolution southern China in 2013.

The ground-based measurements of air temperature, VPD, SWC and GPP at Lishui site from 2012 to 2013 are shown in Fig. S4. The air temperature and VPD in summer 2013 are much higher than those in summer 2012. The GPP has large reductions coincided with reduced soil moisture at Lishui site during the heatwave. The results from the eddy tower confirm the substantial impacts of heatwave on vegetation growth in southern China.

3.3. The impacts of soil moisture and VPD on vegetation growth

The relationships between vegetation growth and VPD and soil moisture are investigated in this part. The normalized monthly SIF_{yield} anomalies show a positive correlation with SWC anomalies in Yunnan ($R = 0.29$, $p < 0.001$) and southern China ($R = 0.39$, $p < 0.001$) (Fig. 7a). The remote-sensed soil moisture only indicates the water condition in the surface soil, and vegetation growth is also strongly affected by the soil moisture in the root zone. TWS can provide information on soil moisture in deep layers and groundwater storage. Therefore, the relationships between TWS and SIF_{yield} are shown in Fig. 7b. The monthly SIF_{yield} anomalies show a positive correlation with the TWS anomalies in Yunnan ($R = 0.27$, $p < 0.001$) and southern China ($R = 0.21$, $p < 0.001$), which is similar to the results found for SWC. However, the VPD-SIF_{yield} correlations tend to be stronger (Fig. 7c), and the temporal correlations are -0.58 and -0.68 in Yunnan and southern China,

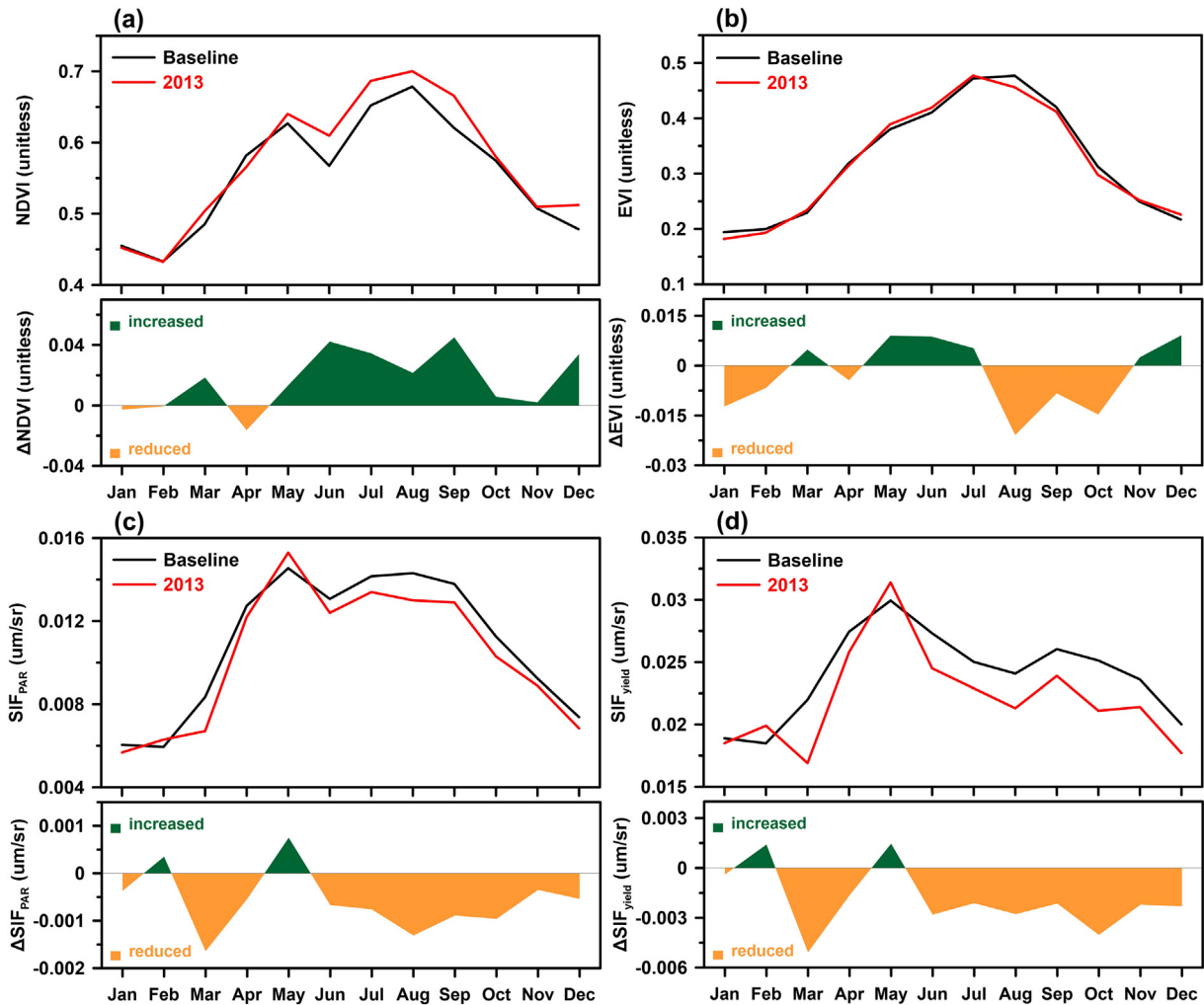


Fig. 6. The region-wide mean seasonal cycle and anomalies of (a) NDVI, (b) EVI, (c) SIF_{PAR} and (d) SIF_{yield} for southern China in 2013. The black curves represent the monthly multiyear mean of each variable between 2007 and 2016; the red curves show the seasonal evolution during the heatwave period. (For interpretation of the references to colour in this figure legend, the reader is referred to the web version of this article.)

respectively. The temporal correlations between SIF_{yield} and VPD anomalies are stronger than those between SIF_{yield} and soil water in the surface and deep layers in both study areas.

The relationships between SIF_{yield} and VPD and soil moisture are further investigated at the spatial scale. The SCCs between SIF_{yield} and the

SWC, TWS, and VPD anomalies during the drought and heatwave events are shown in Fig. S5. The results show that the spatial distributions between SIF_{yield} and VPD generally show higher similarities than those between SIF_{yield} and SWC and TWS during the drought and heatwave. Overall, the analysis shows that the VPD- SIF_{yield} correlations tend to

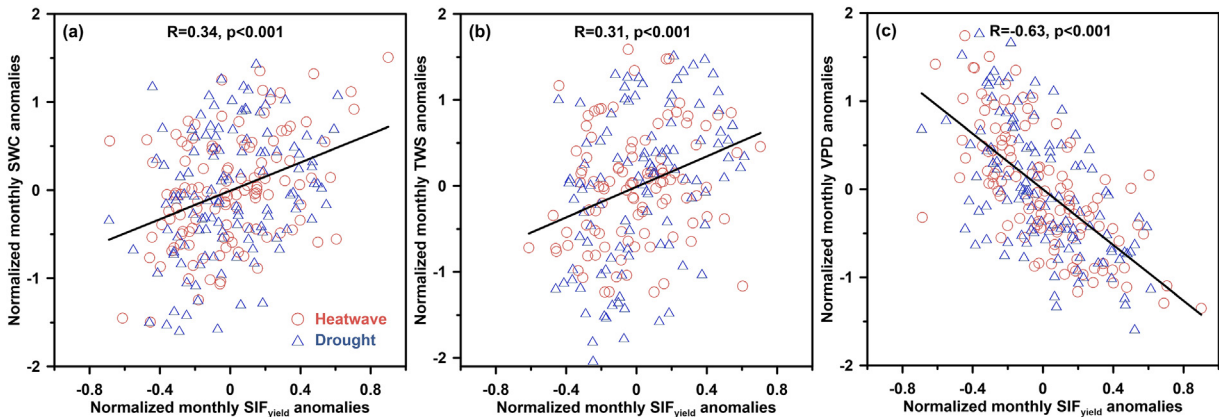


Fig. 7. Relationships between the SIF_{yield} anomalies and climate variable anomalies in different regions. (a) Normalized monthly SIF_{yield} anomalies versus ESA SWC anomalies; (b) normalized monthly SIF_{yield} anomalies versus TWS anomalies; (c) normalized monthly SIF_{yield} anomalies versus TWS anomalies. The correlation coefficients (R) and associated p values provided in each figure are calculated by pooling together all the data in the two study regions.

be stronger at spatial and temporal scales when vegetation experiences water and heat stresses in both areas.

4. Discussion

4.1. Potential of using SIF for drought and heatwave monitoring

The temporal and spatial variations in SIF_{PAR} and SIF_{yield} during the drought and heatwave periods improved our understanding of the mechanisms of drought and heatwave in southern China. Compared to the traditional greenness-based VIs, SIF_{PAR} and SIF_{yield} show better abilities to capture the dynamics process of water and heat stress developments. Our results in this paper are consistent with the results of previous studies that have shown that satellite SIF observations can be used as a direct proxy for photosynthesis (Qian et al., 2019; Smith et al., 2018; Sun et al., 2017).

The timely and accurate monitoring of water and heat stress could better estimate their threats to terrestrial ecosystems. Traditional greenness-based VIs have limitations for drought and heatwave monitoring. Our results demonstrated that NDVI and EVI showed a small increase, but the photosynthesis capacity was reduced at the early drought or heatwave stage (Figs. 2 and 6), indicating that VIs are less sensitive to environmental stress. Yang et al. (2018) also found the photosynthesis in the rainforest was suppressed by water stress, while the canopy greenness was still increased. These traditional VIs only describe the potential photosynthesis and are not directly linked to actual photosynthesis processes (Lee et al., 2013; Meroni et al., 2008).

SIF has a physiological link to photosynthetic activity and a higher sensitivity to the environmental stress than traditional VIs. Therefore, SIF can be used as a good indicator to monitor and assess the impacts of droughts and heatwaves on vegetation growth. Lee et al. (2013) found that drought events have large impacts on satellite SIF observations over tropical rain forests, while NDVI did not respond well to water stress. Guan et al. (2016) demonstrated that using the GPP derived from GOME-2 SIF data can provide better estimations of crop yield compared to greenness-based VIs in the United States. In the Indian Indo-Gangetic Plains, Song et al. (2018) found that SIF observations exhibited a clear response to the heat stress at the early stage of the heatwave, while VIs began to show the reductions about one month later. Our results also show that SIF_{PAR} and SIF_{yield} exhibit earlier reductions than NDVI and EVI at the early stage of the drought and heatwave. As there are lags in the response to water and heat stress from the traditional VIs (Wang et al., 2003), satellite SIF products show great potential for drought and heatwave monitoring and can be used to estimate the impacts of water and heat stress on vegetation growth in a timely manner (Guan et al., 2016; Lee et al., 2013; Sun et al., 2015; Yoshida et al., 2015).

Besides the GOME-2 SIF products, existing instruments include Orbiting Carbon Observatory-2 (OCO-2) (Sun et al., 2018), the TROPOspheric Monitoring Instrument (TROPOMI) onboard Sentinel-5 Precursor (Guanter et al., 2015) and Atmospheric Carbon dioxide Grating Spectroradiometer (AGCS) module onboard Chinese Carbon Dioxide Observation Satellite Mission (TanSat) (Du et al., 2018). And there are some upcoming missions such as the ESA Fluorescence Explorer (FLEX) (Drusch et al., 2017). These satellite SIF measurements with higher spatial and temporal resolution will provide a unique opportunity to have more accurate evaluations of the impacts of drought and heatwave on terrestrial ecosystems in the near future.

4.2. Impacts of soil moisture and atmospheric aridity on the carbon cycle

Many studies have revealed the impacts of drought and heatwave on vegetation growth. Our results show that in the early stage of the water and heat stress, the VPD increases and soil moisture decreases, leading to stomatal closure and a decrease in the photosynthetic functioning of vegetation in both study areas (Figs. 2 and 6). Increased atmospheric

aridity and decreased soil moisture have been used as two key variables in controlling the carbon uptake of terrestrial ecosystems (Katul et al., 2009). Vegetation tends to reduce stomatal conductance and water loss at high VPD values (Katul et al., 2009). Previous studies also found that the photosynthetic rates exhibited substantial declines when the plants experienced high temperatures even for a short time (Al-Khatib and Paulsen, 1990). Decreased soil moisture also triggers plant stomata to partially close to prevent hydraulic conductivity loss (Martínez-Vilalta et al., 2014). Qiu et al. (2018) found that the wilting point, which is the key coupler between the carbon and water cycles, is a crucial parameter for the SIF simulation in land surface models.

Recent studies based on observational data and modeled simulations have shown that vegetation growth may be more sensitive to high VPD than to low soil moisture (Lobell et al., 2014; Novick et al., 2016). To disentangle the impacts of these two drivers on ecosystem carbon uptake when plants experience water and heat stress, we examine the relationships between SIF_{yield} and VPD and soil moisture at the spatial and temporal scales in Yunnan and southern China. Our analysis demonstrates that the VPD-SIF_{yield} correlations tend to be stronger at spatial and temporal scales when the vegetation experiences water and heat stresses in both areas. In the future, droughts and heatwaves will continue to be substantial threats to terrestrial ecosystems and warmer temperatures will increase the relative importance of the VPD in limiting terrestrial carbon uptake (Novick et al., 2016).

4.3. Differential drought and heatwave dynamics

This work demonstrates that satellite SIF reasonably captures the spatial and temporal variations in vegetation growth during the drought and heatwave events. The onset of drought follows a strong soil moisture deficit and VPD increase due to the yearlong below-normal precipitation in Yunnan from 2009 to 2010 (Fig. 1). The onset of the 2013 heatwave in southern China follows relatively higher temperatures and precipitation in late spring but a sudden temperature increase and rainfall deficit in summer (Fig. 4). Such differences in drought and heatwave onset dynamics lead to different VPD and soil moisture variations, which may have different influences on the development of vegetation growth. For drought, the yearlong rainfall deficit results in strong water stress for vegetation growth in Yunnan that lasts for a long time (Zhang et al., 2012). For heatwave, the photosynthetic activity in summer is suppressed by the sudden VPD increase induced by the extremely high air temperature (Yuan et al., 2016). In addition, the increased vegetation productivity in late spring is stimulated by favorable temperature and water conditions and the positive carbon cycle in spring enhances the water limitations caused by sudden precipitation depletion later in the summer (Sun et al., 2015; Wolf et al., 2016). Satellite-based SIF data can adequately capture the response of vegetation to water and heat stress and improve the understanding of the evolution of drought and heatwave.

5. Conclusions

In this paper, we use satellite SIF observations along with other meteorological and vegetation datasets to investigate the impacts of extreme droughts and heatwaves on plant photosynthesis in southern China. Our results demonstrate that SIF can be an effective indicator to monitor heat and water stress in vegetation across southern China. Satellite SIF_{PAR} and SIF_{yield} show more pronounced responses to precipitation deficits and high temperatures than traditional VIs, which underestimate the losses by approximately 50%. Moreover, SIF_{PAR} and SIF_{yield} indicate losses in response to heat and water stress approximately one month earlier in the early drought and heatwave stage compared to the greenness VIs. The early and pronounced responses of the SIF observations to droughts and heatwaves indicate high sensitivity to variations in canopy structure and physiological processes. The VPD-SIF_{yield} correlations tend to be stronger at spatial and temporal

scales when vegetation experiences water and heat stresses in both areas. This study highlights the great potential of using satellite SIF observations to monitor drought and heatwave in the future.

Acknowledgements

This research is financially supported by the National Key Research and Development Program of China (2017YFA0603803), Natural Science Foundation of China (41705056), the Natural Science Foundation of Jiangsu Province (BK20170638) and China Postdoctoral Science Foundation (2017M621698, 2018T110477). The authors acknowledge the China Meteorological Administration for the meteorological station data, the National Aeronautics and Space Administration for the SIF data, the Jet Propulsion Laboratory for the GRACE data, and the NASA Langley Research Center for the PAR data, the Global Inventory Modeling and Mapping Studies (GIMMS) group for the NDVI data. All the MODIS data used in this study were obtained from the NASA LP DAAC. ESA CCI soil moisture data can be accessed through <ftp://anon-ftp.ceda.ac.uk/neodc/esacci/>. GLEAM soil moisture dataset is freely available on VU university Amsterdam Geoservices website <http://geoservices.falw.vu.nl>.

Appendix A. Supplementary data

Supplementary data to this article can be found online at <https://doi.org/10.1016/j.scitotenv.2019.133627>.

References

- Al-Khatib, K., Paulsen, G.M., 1990. Photosynthesis and productivity during high-temperature stress of wheat genotypes from major world regions. *Crop Sci.* 30, 1127–1132.
- Chen, J.L., Wilson, C.R., Tapley, B.D., Ries, J.C., 2004. Low degree gravitational changes from GRACE: validation and interpretation. *Geophys. Res. Lett.* 31.
- Ciais, P., Reichstein, M., Viovy, N., Granier, A., Ogee, J., Allard, V., Aubinet, M., Buchmann, N., Bernhofer, C., Carrara, A., 2005. Europe-wide reduction in primary productivity caused by the heat and drought in 2003. *Nature* 437, 529.
- Dai, A., 2013. Increasing drought under global warming in observations and models. *Nat. Clim. Chang.* 3, 52–58.
- Dong, X., Minnis, P., Xi, B., Sun-Mack, S., Chen, Y., 2008. Comparison of CERES-MODIS stratus cloud properties with ground-based measurements at the DOE ARM Southern Great Plains site. *J. Geophys. Res. Atmos.* 113.
- Dorigo, W.A., Gruber, A., De Jeu, R.A.M., Wagner, W., Stacke, T., Loew, A., Albergel, C., Brocca, L., Chung, D., Parinussa, R.M., 2015. Evaluation of the ESA CCI soil moisture product using ground-based observations. *Remote Sens. Environ.* 162, 380–395.
- Drusch, M., Moreno, J., Del Bello, U., Franco, R., Goulas, Y., Huth, A., Kraft, S., Middleton, E.M., Miglietta, F., Mohammed, G., 2017. The fluorescence explorer mission concept –ESA's Earth explorer 8. *IEEE Trans. Geosci. Remote Sens.* 55, 1273–1284.
- Du, S., Liu, L., Liu, X., Zhang, Xiao, Zhang, Xingyng, Bi, Y., Zhang, L., 2018. Retrieval of global terrestrial solar-induced chlorophyll fluorescence from TanSat satellite. *Sci. Bull.* 63, 1502–1512.
- Guan, K., Berry, J.A., Zhang, Y., Joiner, J., Guanter, L., Badgley, G., Lobell, D.B., 2016. Improving the monitoring of crop productivity using spaceborne solar-induced fluorescence. *Glob. Chang. Biol.* 22, 716–726.
- Guanter, L., Aben, I., Tol, P., Krijger, J.M., Hollstein, A., Köhler, P., Damm, A., Joiner, J., Frankenberg, C., Landgraf, J., 2015. Potential of the TROPOMI monitoring instrument (TROPOMI) onboard the Sentinel-5 precursor for the monitoring of terrestrial chlorophyll fluorescence. *Atmos. Meas. Tech.* 8, 1337–1352.
- Guo, W., Wang, X., Sun, J., Ding, A., Zou, J., 2016. Comparison of land-atmosphere interaction at different surface types in the mid-to lower reaches of the Yangtze River valley. *Atmos. Chem. Phys.* 16, 9875–9890.
- Joiner, J., Yoshida, Y., Guanter, L., Middleton, E.M., Huemmrich, K.F., Yoshida, Y., Frankenberg, C., 2013. Global monitoring of terrestrial chlorophyll fluorescence from moderate-spectral-resolution near-infrared satellite measurements: methodology, simulations, and application to GOME-2. *Atmos. Meas. Tech.* 6, 2803–2823.
- Joiner, J., Yoshida, Y., Guanter, L., Middleton, E.M., 2016. New methods for the retrieval of chlorophyll red fluorescence from hyperspectral satellite instruments: simulations and application to GOME-2 and SCIAMACHY. *Atmos. Meas. Tech.* 9.
- Katul, G.G., Palmroth, S., Oren, R.A.M., 2009. Leaf stomatal responses to vapour pressure deficit under current and CO₂-enriched atmosphere explained by the economics of gas exchange. *Plant Cell Environ.* 32, 968–979.
- Lee, J.-E., Frankenberg, C., van der Tol, C., Berry, J.A., Guanter, L., Boyce, C.K., Fisher, J.B., Morrow, E., Worden, J.R., Asefi, S., 2013. Forest productivity and water stress in Amazonia: observations from GOSAT chlorophyll fluorescence. *Proc. R. Soc. B Biol. Sci.* 280, 20130171.
- Li, Q., Liu, X., Zhang, H., 2004. Detecting and adjusting temporal inhomogeneity in Chinese mean surface air temperature data. *Adv. Atmos. Sci.* 21, 260.
- Liu, Y.Y., Dorigo, W.A., Parinussa, R.M., de Jeu, R.A.M., Wagner, W., McCabe, M.F., Evans, J.P., Van Dijk, A., 2012. Trend-preserving blending of passive and active microwave soil moisture retrievals. *Remote Sens. Environ.* 123, 280–297.
- Lobell, D.B., Roberts, M.J., Schlenker, W., Braun, N., Little, B.B., Rejesus, R.M., Hammer, G.L., 2014. Greater sensitivity to drought accompanies maize yield increase in the US Midwest. *Science* 344, 516–519 80..
- Martens, B., Miralles, D.G., Lievens, H., Van Der Schalie, R., De Jeu, R.A.M., Fernández-Prieto, D., Beck, H.E., Dorigo, W.A., Verhoest, N.E.C., 2017. GLEAM v3: satellite based land evaporation and root-zone soil moisture. *Geosci. Model Dev.* 10 (5), 1903–1925.
- Martínez-Vilalta, J., Poyatos, R., Aguadé, D., Retana, J., Mencuccini, M., 2014. A new look at water transport regulation in plants. *New Phytol.* 204, 105–115.
- Meroni, M., Rossini, M., Picchi, V., Panigada, C., Cogliati, S., Nali, C., Colombo, R., 2008. Assessing steady-state fluorescence and PRI from hyperspectral proximal sensing as early indicators of plant stress: the case of ozone exposure. *Sensors* 8, 1740–1754.
- Miralles, D.G., De Jeu, R.A.M., Gash, J.H., Holmes, T.R.H., Dolman, A.J., 2011. Magnitude and variability of land evaporation and its components at the global scale. *Hydrol. Earth Syst. Sci.* 15, 967–981.
- Myneni, R.B., Hoffman, S., Knyazikhin, Y., Privette, J.L., Glassy, J., Tian, Y., Wang, Y., Song, X., Zhang, Y., Smith, G.R., 2002. Global products of vegetation leaf area and fraction absorbed PAR from year one of MODIS data. *Remote Sens. Environ.* 83, 214–231.
- Novick, K.A., Ficklin, D.L., Stoy, P.C., Williams, C.A., Bohrer, G., Oishi, A.C., Papuga, S.A., Blanken, P.D., Noormets, A., Sulman, B.N., 2016. The increasing importance of atmospheric demand for ecosystem water and carbon fluxes. *Nat. Clim. Chang.* 6, 1023.
- Pinzon, J.E., Tucker, C.J., 2014. A non-stationary 1981–2012 AVHRR NDVI3g time series. *Remote Sens.* 6, 6929–6960.
- Porcar-Castell, A., Tyystjärvi, E., Atherton, J., Van der Tol, C., Flexas, J., Pfundel, E.E., Moreno, J., Frankenberg, C., Berry, J.A., 2014. Linking chlorophyll a fluorescence to photosynthesis for remote sensing applications: mechanisms and challenges. *J. Exp. Bot.* 65, 4065–4095.
- Qian, X., Qiu, B., Zhang, Y., 2019. Widespread decline in vegetation photosynthesis in Southeast Asia due to the prolonged drought during the 2015/2016 El Niño. *Remote Sens.* 11, 910.
- Qiu, B., Xue, Y., Fisher, J.B., Guo, W., Berry, J.A., Zhang, Y., 2018. Satellite chlorophyll fluorescence and soil moisture observations lead to advances in the predictive understanding of global terrestrial coupled carbon-water cycles. *Glob. Biogeochem. Cycles* 32, 360–375.
- Qiu, B., Li, W., Wang, X., Shang, L., Song, C., Guo, W., Zhang, Y., 2019. Satellite-observed solar-induced chlorophyll fluorescence reveals higher sensitivity of alpine ecosystems to snow cover on the Tibetan Plateau. *Agric. For. Meteorol.* 271, 126–134.
- Reichstein, M., Ciais, P., Papale, D., Valentini, R., Running, S., Viovy, N., Cramer, W., Granier, A., Ogee, J., Allard, V., 2007. Reduction of ecosystem productivity and respiration during the European summer 2003 climate anomaly: a joint flux tower, remote sensing and modelling analysis. *Glob. Chang. Biol.* 13, 634–651.
- Smith, W.K., Biederman, J.A., Scott, R.L., Moore, D.J.P., He, M., Kimball, J.S., Yan, D., Hudson, A., Barnes, M.L., MacBean, N., 2018. Chlorophyll fluorescence better captures seasonal and interannual gross primary productivity dynamics across dryland ecosystems of southwestern North America. *Geophys. Res. Lett.* 45, 748–757.
- Song, L., Guanter, L., Guan, K., You, L., Huete, A., Ju, W., Zhang, Y., 2018. Satellite sun-induced chlorophyll fluorescence detects early response of winter wheat to heat stress in the Indian Indo-Gangetic Plains. *Glob. Chang. Biol.* 24, 4023–4037.
- Sun, Y., Fu, R., Dickinson, R., Joiner, J., Frankenberg, C., Gu, L., Xia, Y., Fernando, N., 2015. Drought onset mechanisms revealed by satellite solar-induced chlorophyll fluorescence: insights from two contrasting extreme events. *J. Geophys. Res. Biogeosci.* 120, 2427–2440.
- Sun, Y., Frankenberg, C., Wood, J.D., Schimel, D.S., Jung, M., Guanter, L., Drewry, D.T., Verma, M., Porcar-Castell, A., Griffis, T.J., 2017. OCO-2 advances photosynthesis observation from space via solar-induced chlorophyll fluorescence. *Science* 358 80–eaam5747.
- Sun, Y., Frankenberg, C., Jung, M., Joiner, J., Guanter, L., Köhler, P., Magney, T., 2018. Overview of Solar-Induced chlorophyll Fluorescence (SIF) from the Orbiting Carbon Observatory-2: retrieval, cross-mission comparison, and global monitoring for GPP. *Remote Sens. Environ.* 209, 808–823.
- Trenberth, K.E., Dai, A., Van Der Schrier, G., Jones, P.D., Barichivich, J., Briffa, K.R., Sheffield, J., 2014. Global warming and changes in drought. *Nat. Clim. Chang.* 4, 17.
- Wahr, J., Swenson, S., Zlotnicki, V., Velicogna, I., 2004. Time-variable gravity from GRACE: first results. *Geophys. Res. Lett.* 31.
- Wang, J., Rich, P.M., Price, K.P., 2003. Temporal responses of NDVI to precipitation and temperature in the central Great Plains, USA. *Int. J. Remote Sens.* 24, 2345–2364.
- Wang, X., Guo, W., Qiu, B., Liu, Y., Sun, J., Ding, A., 2017a. Quantifying the contribution of land use change to surface temperature in the lower reaches of the Yangtze River. *Atmos. Chem. Phys.* 17, 4989–4996.
- Wang, P., Tang, J., Sun, X., Wang, S., Wu, J., Dong, X., Fang, J., 2017b. Heat waves in China: definitions, leading patterns, and connections to large-scale atmospheric circulation and SSTs. *J. Geophys. Res. Atmos.* 122, 10–679.
- Wolf, S., Keenan, T.F., Fisher, J.B., Baldocchi, D.D., Desai, A.R., Richardson, A.D., Scott, R.L., Law, B.E., Litvak, M.E., Brunsell, N.A., 2016. Warm spring reduced carbon cycle impact of the 2012 US summer drought. *Proc. Natl. Acad. Sci.* 113, 5880–5885.
- Xu, L., Samanta, A., Costa, M.H., Ganguly, S., Nemani, R.R., Myneni, R.B., 2011. Widespread decline in greenness of Amazonian vegetation due to the 2010 drought. *Geophys. Res. Lett.* 38.
- Yang, J., Tian, H., Pan, S., Chen, G., Zhang, B., Dangal, S., 2018. Amazon drought and forest response: largely reduced forest photosynthesis but slightly increased canopy greenness during the extreme drought of 2015/2016. *Glob. Chang. Biol.* 24, 1919–1934.

- Yoshida, Y., Joiner, J., Tucker, C., Berry, J., Lee, J.-E., Walker, G., Reichle, R., Koster, R., Lyapustin, A., Wang, Y., 2015. The 2010 Russian drought impact on satellite measurements of solar-induced chlorophyll fluorescence: insights from modeling and comparisons with parameters derived from satellite reflectances. *Remote Sens. Environ.* 166, 163–177.
- Yuan, W., Cai, W., Chen, Y., Liu, S., Dong, W., Zhang, H., Yu, G., Chen, Z., He, H., Guo, W., 2016. Severe summer heatwave and drought strongly reduced carbon uptake in Southern China. *Sci. Rep.* 6, 18813.
- Zhang, L., Zhou, T., 2015. Drought over East Asia: a review. *J. Clim.* 28, 3375–3399.
- Zhang, L., Xiao, J., Li, J., Wang, K., Lei, L., Guo, H., 2012. The 2010 spring drought reduced primary productivity in southwestern China. *Environ. Res. Lett.* 7, 45706.
- Zhang, Y., Joiner, J., Gentine, P., Zhou, S., 2018. Reduced solar-induced chlorophyll fluorescence from GOME-2 during Amazon drought caused by dataset artifacts. *Glob. Chang. Biol.* 24, 2229–2230.
- Zhao, M., Running, S.W., 2010. Drought-induced reduction in global terrestrial net primary production from 2000 through 2009. *Science* 329, 940–943 80–.
- Zhou, L., Tian, Y., Myneni, R.B., Ciais, P., Saatchi, S., Liu, Y.Y., Piao, S., Chen, H., Vermote, E.F., Song, C., 2014. Widespread decline of Congo rainforest greenness in the past decade. *Nature* 509, 86.